

# Lab Report S261

## Optical Astronomy and Gravitational Lensing

Jonathan Burke, Charles Giese

September 2022

### Abstract

The aim of this experiment was to provide an introduction to optical astronomical observational and data reduction techniques. This was done in two parts. Firstly, carrying out data reduction on observations previously made of a gravitationally lensed quasar systems, and determine the time delay between the different light travel paths in order to constrain the value of the Hubble parameter. It was found that the time delay between the two gravitationally lensed images of quasar SDSS1650+4251 was  $36.7 \pm 4.6$  days. From this the value for the Hubble parameter was found to be  $H_0 = 73.4 \pm 5 \text{ kmMpc}^{-1}\text{s}^{-1}$ , which agrees with previous work found in literature.

Using the 50cm Cassegrain telescope in the AIfA, the second half of the transit of the exoplanet TOI 1461.1b was observed during the night of the 24<sup>th</sup> of August 2022. After the data reduction was carried out, a lightcurve was obtained which showed the exoplanet transit. From the lightcurve, it was measured that the exoplanet has a transit magnitude depth of  $0.041 \pm 0.005$ , and the ratio between the planet and host star radii is  $0.0187 \pm 0.0002$ . The value obtained for the magnitude depth is greater than the expected value found in the literature. This was likely caused by issues in calculating the scale factor which overcompensates and increases the magnitude of the star for the later frames of the observations.

# Contents

<b>1</b>	<b>Theory</b>	<b>4</b>
1.1	Astrophysical Theory . . . . .	4
1.1.1	Cosmology . . . . .	4
1.1.2	Gravitational Lensing . . . . .	5
1.1.3	Single Isothermal Sphere(SIS) . . . . .	8
1.1.4	Time Delay . . . . .	8
1.1.5	Quasars . . . . .	8
1.2	Calibration Frames . . . . .	8
1.2.1	Bias . . . . .	8
1.2.2	Dark . . . . .	9
1.2.3	Flat . . . . .	9
<b>2</b>	<b>Preparatory Tasks</b>	<b>10</b>
<b>3</b>	<b>Analysis</b>	<b>12</b>
3.1	Data Reduction . . . . .	12
3.1.1	Raw Image Inspection . . . . .	12
3.1.2	Reduction of R-Band Data . . . . .	13
3.2	PSF Extraction . . . . .	17
3.3	Component Fitting . . . . .	19
3.4	Time-Delay Estimation . . . . .	22
3.5	Lensing Analysis . . . . .	23
<b>I</b>	<b>Night-Time Observations of an Exoplanet Transit</b>	<b>26</b>
<b>4</b>	<b>Theory</b>	<b>26</b>
4.1	Exoplanets . . . . .	26
4.1.1	Exoplanet Discovery Methods . . . . .	26
4.1.2	Geometry of Transits . . . . .	27
<b>5</b>	<b>Preparatory Tasks</b>	<b>28</b>
5.1	Source Selection . . . . .	28
<b>6</b>	<b>Observations</b>	<b>28</b>
<b>7</b>	<b>Analysis</b>	<b>30</b>
7.1	Data Reduction . . . . .	30
7.2	Astrometry . . . . .	31
7.3	Source Fluxes . . . . .	31

<b>8</b>	<b>Results</b>	<b>32</b>
<b>9</b>	<b>Conclusions</b>	<b>35</b>

# 1 Theory

## 1.1 Astrophysical Theory

### 1.1.1 Cosmology

From measuring the redshift of extragalactic objects it was found that almost all objects in the Universe are moving away from us, with increasing velocities at larger distances[4]. This has been interpreted as the Universe expanding. The value of this redshift,  $z$ , is defined using the equation

$$z = \frac{\lambda_{\text{observed}} - \lambda_{\text{emitted}}}{\lambda_{\text{emitted}}} \quad (1)$$

The redshift of a source is related to a quantity called the scale factor  $a(t)$ , which describes the expansion of the Universe as a function of cosmic time  $t$ . The scale factor is normalised to have a current value of unity i.e.  $a(t_0) = 1$ . They are related via the equation

$$a(t) = \frac{1}{1+z} \quad (2)$$

In the 1920s, the astrophysicists Robertson and Walker used Einstein's framework of General relativity to derive the metric for a spatially isotropic and homogeneous Universe.

$$ds^2 = c^2 dt^2 - a^2(t)[dw^2 + f_K^2(w)(d\theta^2 + \sin\theta d\psi^2)] \quad (3)$$

Where  $w$  is the comoving radial coordinate (does not scale with expansion), and  $\theta$  and  $\psi$  are the angular coordinates of a sphere.

The curvature of space-time is described using the term  $K$ . It changes the metric by influencing the values of the term  $f_K(w)$  in the equation above. Current observations indicate that we live in a universe with flat geometry or no curvature ( $K = 0$ ).

$$f_K(w) = \begin{cases} \frac{1}{\sqrt{K}} \sin(\sqrt{K}w) & K > 0 \\ w & K = 0 \\ \frac{1}{\sqrt{-K}} \sinh(\sqrt{-K}w) & K < 0 \end{cases} \quad (4)$$

Due to this cosmic expansion, objects are observed to have a corresponding velocity given by [8]

$$\mathbf{v} = \dot{a}\mathbf{x} = \frac{\dot{a}}{a}\mathbf{r} = H(t)\mathbf{r} \quad (5)$$

This equation, when the current value for the Hubble parameter,  $H_0$ , is used is referred to as the local Hubble Law and is given by  $v = H_0 D$ , where  $D$  is the distance between the observer and source.

The Friedmann-Lemaitre equation describes the expansion of the Universe[11]. It is given by expression below.

$$H^2(t) = H_0^2 \left[ \frac{\Omega_r}{a^4(t)} + \frac{\Omega_m}{a^3(t)} + \frac{1 - \Omega_m - \Omega_r - \Omega_\Lambda}{a^2(t)} + \Omega_\Lambda \right] \quad (6)$$

The expansion history of the Universe depends on the contribution that each component makes to the total energy content of the Universe. These contributions are expressed using  $\Omega_m$ ,  $\Omega_r$  and  $\Omega_\Lambda$ , which correspond to the contribution from matter, radiation and vacuum energy respectively. The curvature

of space-time contributes through the  $(1 - \Omega_m - \Omega_r - \Omega_\Lambda)$  component. However, current observations indicate that the Universe is flat, and for a flat universe this component is equal to zero and therefore, can be omitted. Matter and radiation have a different dependence on the scale factor due to the fact that for matter, the number density of particles changes proportionally to  $a^{-3}$  as the number of particles is unchanged in a comoving volume, a volume which factors out the expansion of the Universe. For radiation, the number density of photons is unchanged in a comoving volume meaning that it is proportional to  $a^{-3}$ , however, due to the photon getting redshifted, there is an additional factor of  $a^{-1}$ , meaning that the photon energy contribution is proportional to  $a^{-4}$ .

In Euclidean (flat) space, distances are quite easily determined as the separation between two points. For a non-Euclidean space such as our Universe with expanding spacetime, it is not as simple, and therefore, different distance measurement methods result in different values for the distance between two points. On small scales our Universe appears flat and Euclidean and therefore the distance measurements have negligible differences, however, on cosmological scales they can result in very different values[11]. The luminosity distance relates the observed flux,  $S$ , of an object to its luminosity,  $L$ . This distance measurement method requires objects of known luminosity, such Type Ia supernovae. It is given by the following equation [8].

$$D_{lum}(z) = \sqrt{\frac{L}{4\pi S}} \quad (7)$$

The second method of distance measurement is known as the angular diameter distance. This method relates the physical diameter,  $2R$ , of a source to its observed angular diameter  $\theta$ . This method requires objects of known size. It is this distance measurement that is used in gravitational lensing theory. It is given by the following equation [8].

$$D_{ang}(z) = \frac{2R}{\theta} = a(z)f_K(w) \quad (8)$$

This equation for the angular diameter distance can be further expanded upon to give the angular diameter distance of an object at  $z_2$  observed from a redshift of  $z_1$ .

$$D_{ang}(z_1, z_2) = a(z_2)f_K[w(z_2) - w(z_1)] \quad (9)$$

$$= \frac{1}{1+z_2}f_K\left[\frac{c}{H_0}\int_{z_1}^{z_2}\frac{dz'}{\sqrt{(1-\Omega_m-\Omega_\Lambda)(1+z')^2+\Omega_m(1+z')^3+\Omega_\Lambda}}\right] \quad (10)$$

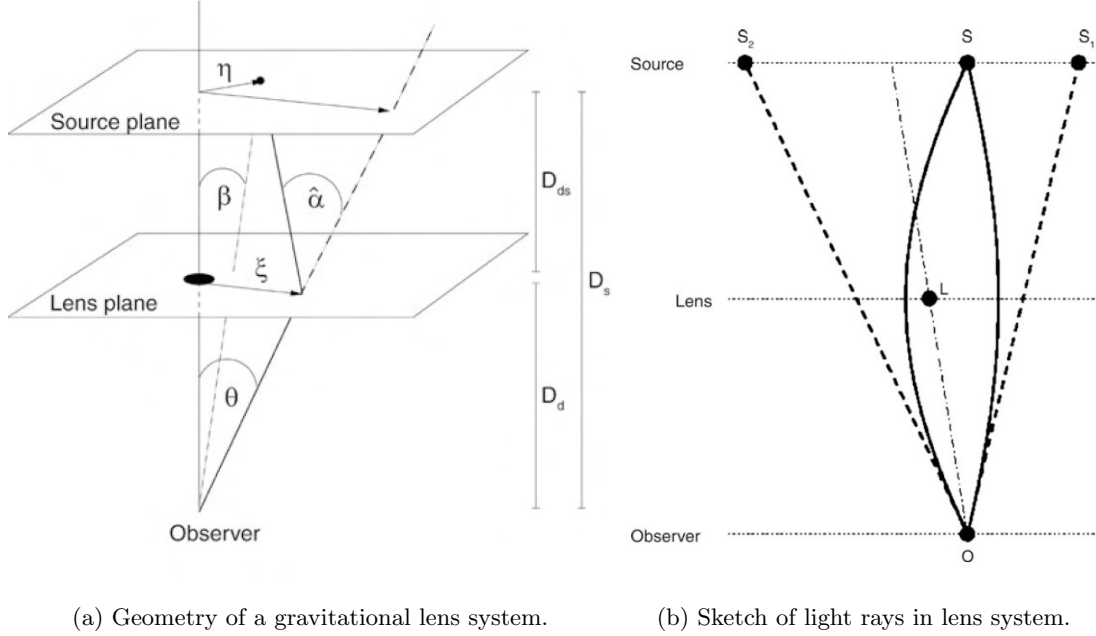
The two distance measurements are related through the expression:

$$D_{lum}(z) = (1+z)^2 D_{ang}(z) \quad (11)$$

### 1.1.2 Gravitational Lensing

Similar to massive particles, the path taken by photons is influenced by the presence of gravitational fields. This is due to the fact that according to the theory of General Relativity, photons propagate along null geodesics of the space-time metric[8]. Figure 1b illustrates how this effect can influence the apparent position of sources. In this experiment, a simplified theory was used which made the two following assumptions. Firstly, the small angle approximation was used. Secondly, the Born approximation was used, which states that the source and lens exist in parallel planes and that the light rays travel in straight

lines, except for when they cross the lens plane where they can be deflected. This is referred to as a geometrically thin lens. This simplified theory can be adopted due to the fact that the distances between the source and lens, and the observer and the lens are significantly larger than the sizes of both the lens and source.



(a) Geometry of a gravitational lens system. (b) Sketch of light rays in lens system.

Figure 1: Source: P. Schneider 2006, Extragalactic "Astronomy and Cosmology" [11]

The lens equation describes the relationship between the apparent angular position of a source in the sky,  $\theta$ , the true position of the source,  $\beta$ , and the scaled deflection angle,  $\alpha$  [8].

$$\beta = \theta - \alpha(\theta) \quad (12)$$

These angles are related to physical distances using the below equation, where  $D_d\theta = \xi$ ,  $\eta = D_s\beta$  and the true deflection angle is  $\hat{\alpha}(\xi)$ . These angles and distances are illustrated in Figure 1a.

$$\eta = \frac{D_s}{D_d}\xi - D_{ds}\hat{\alpha}(\xi) \quad (13)$$

The relationship between the scaled or reduced deflection angle,  $\alpha$ , and the true deflection angle,  $\hat{\alpha}$  is given by Equation (14). This relation is used to simplify the lens equation by removing the factor caused by the distance ratios.

$$\alpha(\theta) = \frac{D_{ds}}{D_s}\hat{\alpha}(D_d\theta) \quad (14)$$

The value calculated for the true deflection angle for a pointlike lens with mass  $M$  and a light ray with impact parameter  $\xi$  is twice as large when predicted with General Relativity when compared to Newtonian gravity. It is given by the Equation (15).

$$\hat{\alpha} = \frac{4GM}{c^2\xi^2}\xi \quad (15)$$

This equation can then be expanded to describe the superposition for the mass distribution in the plane of the lens, where  $\Sigma(\boldsymbol{\xi}')$  is the surface mass density.

$$\hat{\alpha} = \frac{4GM}{c^2 \xi^2} \Sigma(\boldsymbol{\xi}') \frac{\boldsymbol{\xi} - \boldsymbol{\xi}'}{|\boldsymbol{\xi} - \boldsymbol{\xi}'|^2} \quad (16)$$

The convergence,  $\kappa(\boldsymbol{\theta})$ , is a measure for the strength of the lens. It determines whether a lensing system creates multiple images. When  $\kappa < 1$ , it is a weak lensing system which cannot produce multiple images. When  $\kappa > 1$ , it is a strong lensing system and it is possible to produce multiple images of a source. The convergence depends on the surface mass density,  $\Sigma(D_d \boldsymbol{\theta})$ , and the critical surface mass density,  $\Sigma_{cr}$ . The convergence is given by Equation (17) [8].

$$\kappa(\boldsymbol{\theta}) = \frac{\Sigma(D_d \boldsymbol{\theta})}{\Sigma_{cr}} \quad (17)$$

where,

$$\Sigma_{cr} = \frac{c^2}{4\pi G} \frac{D_s}{D_d D_{ds}} \quad (18)$$

These equations allow for the scaled deflection angle in Equation (14) to be written in terms of only observable angles.

$$\boldsymbol{\alpha}(\boldsymbol{\theta}) = \frac{1}{\pi} \int d^2 \theta' \kappa(\boldsymbol{\theta}') \frac{\boldsymbol{\theta} - \boldsymbol{\theta}'}{|\boldsymbol{\theta} - \boldsymbol{\theta}'|^2} \quad (19)$$

The deflection potential encloses all the information about the distribution of mass in the lens. It is given by the equation:

$$\psi(\boldsymbol{\theta}) = \frac{1}{\pi} \int d^2 \theta' \ln |\boldsymbol{\theta} - \boldsymbol{\theta}'| \quad (20)$$

It is related to the scaled deflection angle and the convergence via the equations:

$$\boldsymbol{\alpha}(\boldsymbol{\theta}) = \nabla \psi(\boldsymbol{\theta}) \quad 2\kappa(\boldsymbol{\theta}) = \Delta \psi(\boldsymbol{\theta}) \quad (21)$$

The Fermat potential is a scalar function of the apparent angular position of the source and its true position. The stationary points of this potential are the solutions for the lens equation, Equation (12). This determines the number of images formed for a certain lens geometry. It is given by [8]:

$$\tau(\boldsymbol{\theta}; \boldsymbol{\beta}) = \frac{1}{2}(\boldsymbol{\beta} - \boldsymbol{\theta})^2 - \psi(\boldsymbol{\theta}) \quad (22)$$

where  $\psi(\boldsymbol{\theta})$  is the deflection potential defined by  $\psi(\boldsymbol{\theta}) = \frac{1}{\pi} \int \kappa(\boldsymbol{\theta}') \ln |\boldsymbol{\theta} - \boldsymbol{\theta}'| d^2 \theta'$ . The Fermat potential is used to classify images. For a fixed value of  $\boldsymbol{\beta}$ , with  $\det \mathcal{A} \neq 0$ , vanishing gradients of  $\tau$  correspond to a solution of the lens equation and an image at  $\boldsymbol{\theta}$ . These images can be minima ( $\det \mathcal{A} > 0, \text{tr} \mathcal{A} > 0$ ), maxima ( $\det \mathcal{A} > 0, \text{tr} \mathcal{A} < 0$ ), or saddle points ( $\det \mathcal{A} < 0$ ). This helps determine the number of images created by a source.

The different rays of light get deflected in different ways which results in the distortion and also magnification of the images. This is described using the Jacobian matrix of the lens mapping,  $\mathcal{A}_{ij}$ , which is also used to define the magnification of an image,  $\mu$ .

$$\mathcal{A}_{ij} = \frac{\partial \beta_i}{\partial \theta_j} \quad \mu = \frac{1}{\det \mathcal{A}} \quad (23)$$

### 1.1.3 Single Isothermal Sphere(SIS)

The Single Isothermal Sphere is a mass distribution model that can be used to describe the lensing galaxy. The surface mass density of this model is described by the equation:

$$\Sigma(\xi) = \frac{\sigma_v^2}{2G\xi} \quad (24)$$

The Einstein radius is defined as the angle within which the mean of convergence is unity. For an SIS the Einstein radius is given as:

$$\theta_E = 4\pi \left( \frac{\sigma_v^2}{c^2} \right) \frac{D_{ds}}{D_s} \quad (25)$$

Combining the surface mass density and the Einstein radius allows for the projected mass inside of the Einstein radius to be calculated.

$$M(\theta < \theta_E) = \pi \theta_E^2 D_d^2 \Sigma_{cr} \quad (26)$$

### 1.1.4 Time Delay

The light originating from the separate images in a gravitationally lensed system have different travel times. The light travels for different times due to the bending of the light ray causing different light travel distances and also because the light travels through a strong gravitational potential. This results a time delay between the two images. This delay is described by the equation below, where  $\theta_A$  and  $\theta_B$  are the positions of the two lensed images.

$$\Delta t = \frac{1+z_d}{c} \frac{D_d D_s}{d_{ds}} [\tau(\theta_A; \beta) - \tau(\theta_B; \beta)] \quad (27)$$

### 1.1.5 Quasars

QUASi-stellar radio sources or QUASARS, are very luminous AGNs which are very visible. The source of their strong luminosity is from the accretion of matter onto the supermassive blackhole located at the centre of their host galaxy, where gravitational energy is rapidly transformed into radiation.

In the optical wavelengths, their luminosity exhibits variations on the scale of a number of days making it easily observable. It is this variation in luminosity that is used to measure the time delay between the two gravitationally lensed images.

## 1.2 Calibration Frames

When optical observations are taken of scientific targets, it is not just scientific frames that are taken but also calibration frames. These frames are used in the initial data reduction to help characterise and account for noise and calibrate and improve the quality of the science frames. They remove various sources of noise, vignetting and also specks of dust or defects in the optical set up or CCD.

### 1.2.1 Bias

Bias frames account for the readout noise of the CCD. The readout electronics in a CCD contribute a characteristic noise to the frames. Bias frames are taken with the shutter closed with no exposure time,



meaning that any variation in readout value for each pixel is caused by the readout electronics. Since this noise is random, a number of bias frames are taken and a master bias frame is created from the median of these images which can then be subtracted from the science frames. At least 10 bias frames are usually required to fully statistically account for this readout electronics noise.

### **1.2.2 Dark**

Dark frames record the electronic noise that occurs in the CCD during the exposure. They account for hot pixels, which accumulate more electrons than others and dead pixels, which accumulate less electrons. They also account for the thermal noise or dark current of the CCD, for CCDs which are cooled via electric cooling rather than liquid nitrogen.

Dark frames are taken by capturing frames with the shutter closed, for an exposure time similar to that of the science frames. The median dark frame is then subtracted from the science frames.

### **1.2.3 Flat**

Flat frames account for issues which lead to ununiform illumination of the CCD. This is mainly from variations in gain or quantum efficiency in the pixels across the CCD. The flat frames flatten the relative response of the pixels to incoming light. Flat frames also compensate for specks of dust present on the lens or CCD which lead to donuts shapes being visible in the images. The science frames are divided by the average of the flat frames.

There are multiple ways to obtain flats. Sky flats are one of the preferred methods. This is done by taking exposures of the twilight sky, where it is uniformly illuminated and there are no stars present. Another method is dome flats, where the telescope is pointed at a white screen located on the inside of the telescope dome, which is uniformly illuminated using a lamp. Sky flats are preferred to dome flats as the screen is difficult to uniformly illuminate and is not located at infinity.

## 2 Preparatory Tasks

### P.3.1: Deflection Potential and Scaled Deflection Angle

The deflection potential,  $\psi(\theta)$ , for a spherically symmetric system is given by

$$\psi(\theta) = 2 \int_0^\theta d\theta' \theta' \kappa(\theta') \ln \left( \frac{\theta}{\theta'} \right) \quad (28)$$

When the surface brightness for an SIS lens,  $\Sigma(D_d)$ , is inserted into the convergence parameter,  $\kappa(\theta)$ , it becomes:

$$\kappa(\theta) = \frac{\sigma_v^2}{2GD_d\theta} \frac{4\pi G}{c^2} \frac{D_d D_{ds}}{D_s} = 2\pi \frac{\sigma_v^2}{c^2} \frac{D_{ds}}{D_s \theta} \quad (29)$$

Plugging this equation for  $\kappa(\theta)$  into the deflection potential equation and using the definition for the Einstein angle for an SIS as described earlier, the deflection potential is given by:

$$\psi(\theta) = 4\pi \frac{\sigma_v^2}{c^2} \frac{D_{ds}}{D_s} \int_0^\theta d\theta' \ln \left( \frac{\theta}{\theta'} \right) \quad (30)$$

$$= \theta_E \theta \quad (31)$$

The scaled deflection angle then follows, where  $\hat{\theta} = \vec{\theta}/\theta$ [FIX]

$$\vec{\alpha}(\vec{\theta}) = \nabla \psi(\theta) = \theta_E \hat{\theta} \quad (32)$$

### P.3.2: Solving Lens Equation

Inserting the scaled deflection angle, obtained from the previous task, into the lens equation results in:

$$\vec{\beta} = \vec{\theta} - \theta_E \frac{\vec{\theta}}{\theta} \quad (33)$$

Multiplying both sides of the above equation by  $\vec{\theta}/\theta$ , both  $\vec{\beta}$  and  $\vec{\theta}$  exist on an even plane and can be facing either the same or opposite directions. Therefore, the scalar product of the two vectors has two solutions,  $\vec{\beta} \cdot \vec{\theta} = \pm \beta \theta$ . Hence, the two solutions to the lens equation are given by:

$$\pm \frac{\theta \beta}{\theta} = \theta - \theta_E \quad (34)$$

$$\theta_{\pm} = \theta_E \pm \beta \quad (35)$$

Therefore, it can be seen that the separation between the images,  $s$ , is related to the Einstein radius,  $\theta_E$ , via the following relation.

$$s = 2\theta_E \quad (36)$$

### P.3.3: Magnification Ratio

As described in the previous section, the magnification of an image is given by  $\mu = (\det \mathcal{A})^{-1}$ . For the case of axial symmetry and using the lens equation, this is then given by:

$$\mu = (\det \mathcal{A})^{-1} = \left( \frac{\beta}{\theta} \frac{d\beta}{d\theta} \right)^{-1} \quad (37)$$

$$= \left( \frac{\theta - \theta_E}{\theta} \right)^{-1} \quad (38)$$

therefore the magnification ratio of the two images is:

$$\Gamma = \frac{\mu_+}{\mu_-} = \frac{1 - \theta_E/\theta_-}{1 - \theta_E/\theta_+} \quad (39)$$

### P.3.4: Time Delay

Using the deflection potential derived earlier, the Fermat potential of an SIS lens can be obtained as follows:

$$\tau(\vec{\beta}, \vec{\theta}) = \frac{1}{2}(\vec{\beta} - \vec{\theta})^2 - \psi(\vec{\theta}) \quad (40)$$

$$\Rightarrow \tau_{\pm} = \frac{1}{2}(\theta_{\pm} \mp \theta_E - \theta_{\pm})^2 - \theta_E \theta \quad (41)$$

$$= \frac{1}{2}\theta_E^2 - \theta_E \theta_{\pm} \quad (42)$$

This then gets inserted into the equation for the time delay.

$$c \cdot \Delta t(\vec{\beta}) = (1 + z_d) \frac{D_d D_s}{D_{ds}} \left[ \tau(\vec{\theta}_+, \vec{\beta}) - \tau(\vec{\theta}_-, \vec{\beta}) \right] \quad (43)$$

$$\Delta t(\beta) = \frac{1 + z_d}{c} \frac{D_d D_s}{D_{ds}} \cdot \theta_E (|\theta_-| - |\theta_+|) \quad (44)$$

### P.3.5: Minimum Dispersion Estimator

The minimum dispersion method is built on the assumption that the functional form between two data points is the same in both functions. This method can be improved upon by applying this minimum dispersion method to smooth continuous functions obtained for each light curve by interpolating between data points. This method would provide an improved time delay estimate.

### P.3.6: Dispersion Function Approximation

The dispersion function can be described using using a Taylor expansion when close to the true time delay,  $\lambda_0$ :

$$D^2(\lambda) = D^2(\lambda_0) + \left. \frac{dD^2}{d\lambda} \right|_{\lambda_0} \cdot (\lambda - \lambda_0) + \left. \frac{d^2 D^2}{d\lambda^2} \right|_{\lambda_0} \cdot (\lambda - \lambda_0)^2 + \mathcal{O}(\lambda^3) \quad (45)$$

The minimum of the dispersion function occurs for the true value of the time delay  $\lambda_0$ , where the first derivative of the dispersion function must vanish. Therefore the higher order terms can be neglected, and the resulting dispersion function has the form of a parabola.

$$D^2(\lambda) = D^2(\lambda_0) + \left. \frac{d^2 D^2}{d\lambda^2} \right|_{\lambda_0} \cdot (\lambda - \lambda_0)^2 \quad (46)$$

## 3 Analysis

### 3.1 Data Reduction

#### 3.1.1 Raw Image Inspection

The first step in the data reduction was to manually inspect the raw science and calibration frames obtained from observations of the SDSS1650+4251 lensed quasar system using the Enzian camera at the Hoher List 1m telescope.

The bias and flat field frames were opened and manually inspected. From the bias images it was found that the average bias level was approximately 200 ADU (Analogue-to-Digital Units). However this bias level was not constant across the field of view. In the middle of the frame it was slightly higher than 200 ADU, and at the top and bottom it was slightly lower, averaging approximately 195 ADU. The small white dots that were present in some but not all flat frames were identified as cosmic rays. These cosmic rays hit the CCD during some exposures resulting in pixels with very high counts.

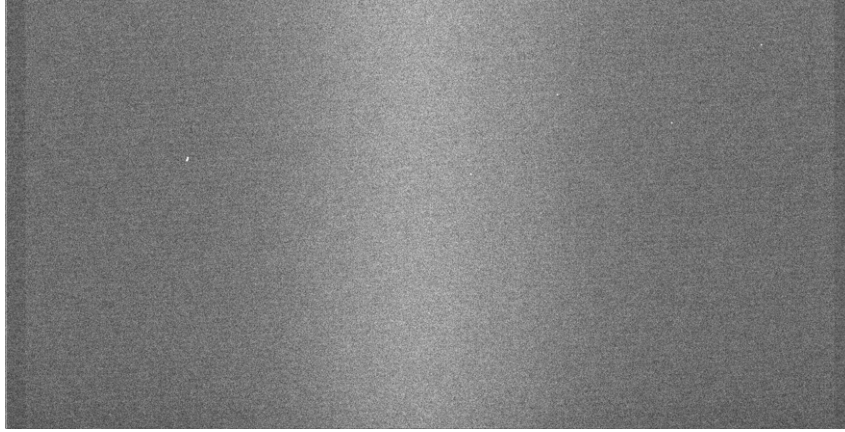
One bias frame was then selected and a region was selected with little large-scale variation in order to compute the background root mean square (rms) value. The area that was selected was a rectangle with x coordinates ranging from 260 to 465 and y coordinates ranging from 190 to 400. The rms value of this region was found to be 1.89 ADU. This bias frame is shown in Figure 2a.

As discussed in Section 1.2, the source of noise in bias frames is the readout electronics of the CCD.

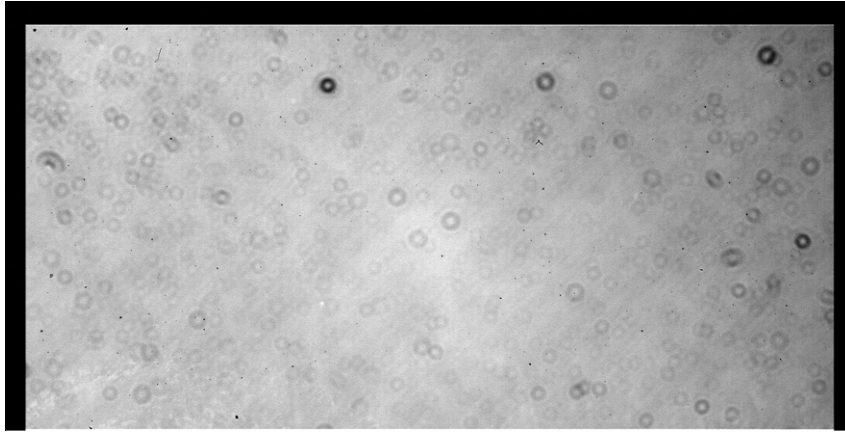
In the flat field frames there are a number of structures visible. There are donut shaped dark regions, sharp irregularly shaped dark structures, and there is also a general inhomogeneity in the background brightness of the image, with one corner being significantly less bright than the other regions of the image. The donut shaped structures are caused by dust or other particles that are on the primary lens of the telescope. Since these obscuring particles are not in focus they cause a projection of the shadow of the secondary mirror to be cast onto the CCD. An example of one of the flat frames is shown in Figure 2b.

In the science frames there are a lot of defects visible, as shown in Figure 2c. As in the flat frames, the defects caused by dust are visible, both from on the lens and on the CCD itself. There is also a vertical stripe of light that is found in some but not all of the science frames, likely bleeding caused by an over saturated pixel. When looking between exposures it can be seen that the location of sources change slightly. This is caused by the fact that the stars move across the sky between exposures and also the telescope dithers between exposures to prevent the same source being collected by the same pixels on the CCD each time, in order to improve accuracy in measurements.

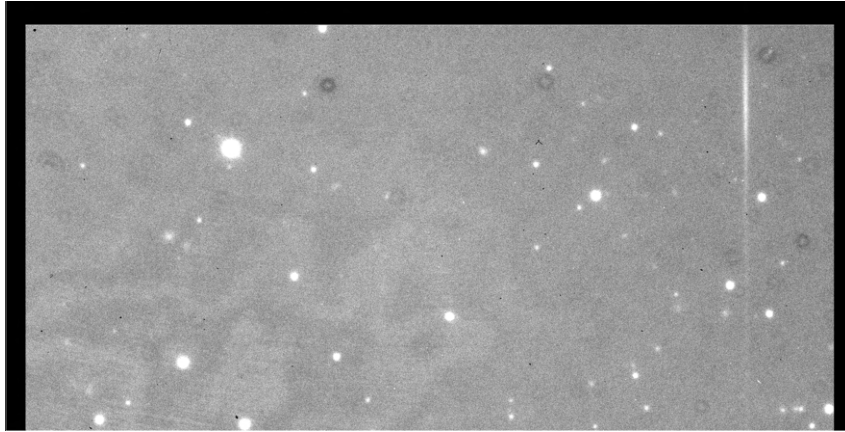
From the first science frame, "image008067.fits", the mean background value was computed for a region without bright objects. This region was selected with x values ranging from 900 to 1150, and y values ranging from 300 to 600. The mean was found to be 675.51 ADU, with an rms value of 19.21 ADU.



(a) Bias Frame



(b) Flat Frame



(c) Science Frame

Figure 2: An example of the raw calibration and science frames.

### 3.1.2 Reduction of R-Band Data

In this analysis, only the images from the R-band filter were used. The software *THELI* was used to perform the data reduction on the science frames provided, as described in Appendix F of the lab manual[8]. *THELI* splits the data reduction into seven stages or processing groups (PG).

The first PG in this process is called *initialise*. This step involved selecting the correct instrument

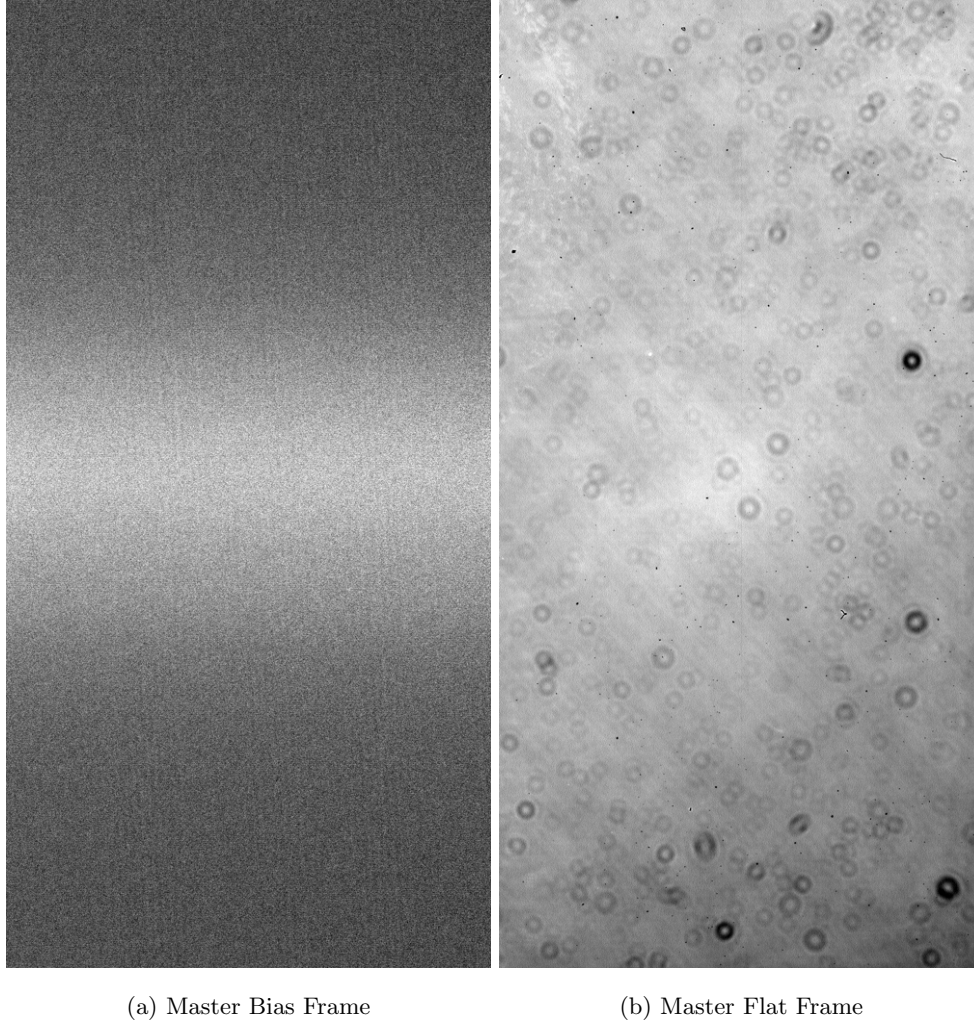


Figure 3: Master bias and master flat frames made by combining the calibration frames.

with which the data was taken. For this section the data was obtained using the Enzian camera at the Hoher List 1m telescope. Then the path to the directories containing the bias, flat and science frames were specified.

The next PG, *preparation*, splits the images or FITS files into single chips, allowing for parallel processing. However, the Enzian camera is a single chip CCD, so the files were not split and only the FITS header was updated. The headers were shortened, and unnecessary information removed from them, and also a number of dummy or empty lines were appended.. The images were also rotated to become vertical instead of horizontal. This can be seen in Figure 3. This was carried out on all the files, calibration and science.

Following this, the *calibration* PG applies the calibration frames to the science in order to reduce the noise and improve the quality of the science frames. This was done in a number of steps. Firstly, the ten bias frames were combined and averaged to produce a master bias frame, shown in Figure 3a. Similarly, the nine flat frames were combined and averaged to create a master flat, shown in Figure 3b. When these master calibration frames are compared against the original frames, such as those shown in Figure 2, a number of differences can be seen. Firstly, the white dots caused by cosmic rays that was present in some

frames have been removed. Also the black edges around the flats have been removed. The contrast in both the flat and bias has been increased. This can be seen in the way that structures such as the donut shapes appear much clearer and sharper than before. This is because the combination of the calibration frames removes the statistical variations in the picture.

The noise dispersion was then computed for the master bias frame for the same region as before. It was found to be 0.32 ADU, which is significantly less than the original of 1.89 ADU. As expected, combining a number of bias frames together reduced the noise dispersion.

The minimum value in the normalised flat field was 0 ADU. Dithering is the process of moving the telescope slightly between exposures. Dithering is important when making observations as it ensures that the same source is not hitting the same pixels for each image. This reduces errors and uncertainties that can arise from quantum efficiency differences between pixels, or reduce the likelihood of a source being hidden behind defective pixels.

These master calibration frames were then applied to the science frames. They were overscan corrected, debiased and flat fielded.

The next PG in this data reduction process is *background*, which models the background from the science frames after they have been bias and flat field calibrated. This is done by creating a superflat from the science frames. *THELI* does this by detecting and masking the objects present in the exposures, and then rescaling and combining them into a median superflat frame, shown in Figure 4a. The object detection method is chosen by specifying the detection threshold per pixel in units of sigma above the sky background noise, and the minimum number of connected pixels that must be above this threshold value. As recommended in the lab manual, values of 1.0 were used for the detection threshold and 10 for the number of connected pixels [8]. The superflat models two things, the fringe model and the illumination model. The fringing occurs from light interference patterns due to slight inhomogeneities in the thickness of the CCD. The illumination model shows how the CCD is unequally illuminated and corrects for this in the science frames. The illumination correction is only slight with it varying approximately 3 ADU from the bright to the dark regions of the model. These models are shown in Figure 4. *THELI* also specifies the way in which this background model is applied. In this instance the divide by smoothed model and subtract fringes option was chosen. After this model was applied to the science frames, the variations due to the the fringing and illumination were removed, however it was only possible to visually observe the fringe pattern being removed as the illumination correction was so small.

Following this, the *weighting* PG was carried out. This was done by normalising the master flat created in a previous PG and detecting bad pixels using threshold pairs. These bad pixels values were replaced by zero. On an image by image basis the remaining hot pixels, CCD defects and cosmics were detected. This process generated weight maps, both a global weight which was applied to all science frames for defects and bad pixels which were constant across all science frames and individual weight maps applied to each frame containing the defects which varied such as cosmic rays.

The next PG, *Astrometry/Photometry*, is the most important of the PGs. Firstly in this process the frames are astrometrically matched to a reference catalogue. This means that the objects in the science frames are correctly matched to their corresponding object in the reference catalogue. The SDSS DR9

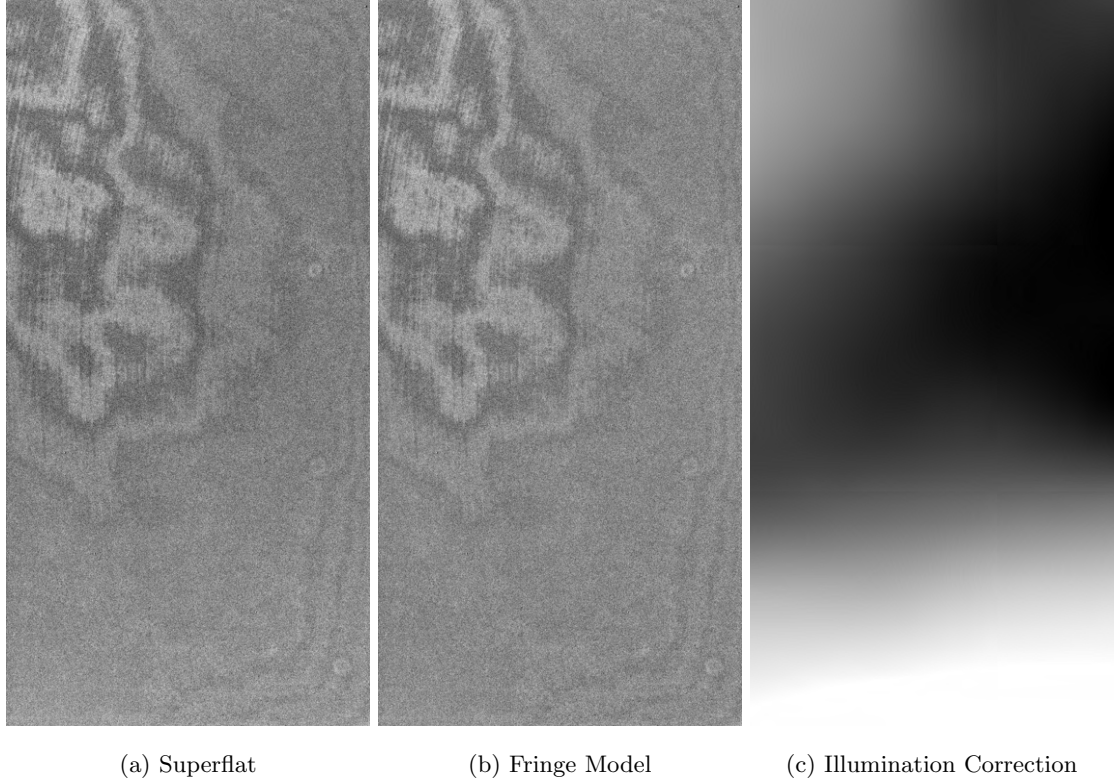


Figure 4: Superflat, fringe model and illumination correction generated from science frames.

catalogue was chosen for this process. *THELI* requires initial reference coordinates for this astrometric matching process, which it automatically obtains from the header of the FITS files. A magnitude limit of 22 mag and a radius limit of 5' were chosen for the matching process. Similar to the previous PG, a source catalogue is created from the science frames, with a detection threshold of  $2\sigma$  and a minimum of ten connected pixels required. This process takes into account the weight maps created previously, to prevent any incorrect detections. *THELI* uses the program *SCAMP* to compare the created source catalogue and the reference catalogue. *SCAMP* was run with the default configurations apart from the `DISTORT_DEGREES` which was set to 1. *SCAMP* produces a WCS (world coordinate system) transformation matrix, which transforms from pixel coordinates on the CCD to sky coordinates. This is used for coaddition process which is done in the next PG.

The final PG, *coaddition*, begins by subtracting a model of the sky from the science frames. The sky model is generated by detecting and masking the objects in the science frames. The detection threshold used was  $1\sigma$ , with a minimum of 10 connected pixels and a kernel width of 256. The remaining image is smoothed and subtracted from the science frames. Then the science frames were coadded in three steps, automatically carried out by the software. The global information about the data set was obtained and reduction settings were made. The science frames and their weight maps were resampled. The resampled images were then combined into a final image.

Figure 5, shows the results from the *coaddition* PG, the final coadded frame and also the coadded weight image. The coadded weight image shows how each of the individual science frames were stacked and also which points were masked due to defects or cosmics. It can be seen that this weight image



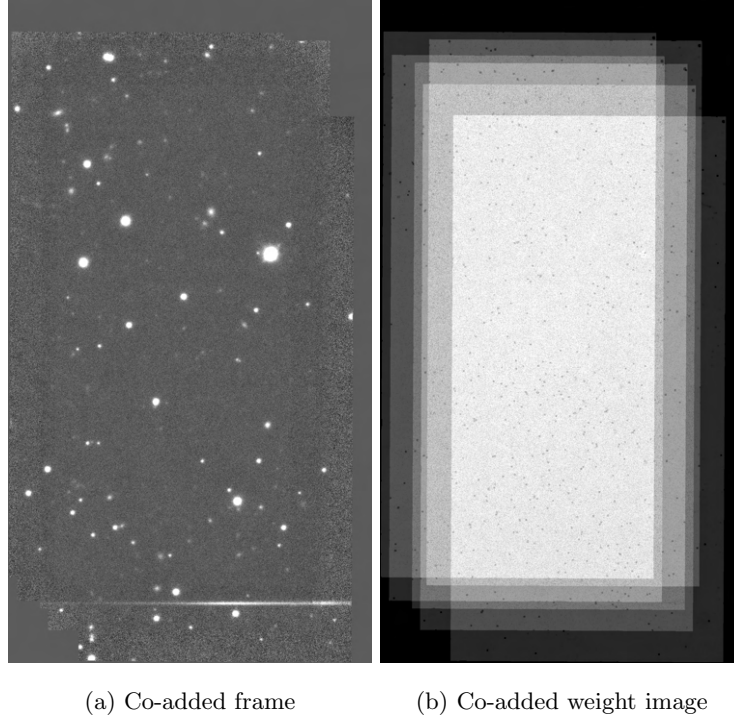


Figure 5: Results from the *coaddition* PG

is related to the background noise of the final coadded science image. The areas with more overlap of frames have a finer structure to the noise compared to the areas of the image where there are less frames overlapping. This was further analysed by computing the noise (rms) for a region in the coadded image that was deeply stacked and did not have any bright objects. The region selected had pixel coordinates with x values ranging from 440 to 640, and y coordinates ranging from 1040 to 1180. The rms noise in this region was found to be 0.02 ADU, which is significantly lower than the single exposure value found earlier which was 19.21 ADU. As expected, the process of applying the calibration frames and using multiple science exposures greatly reduced the noise and allowed for more accurate scientific measurements to be taken from the final coadded science frame.

### 3.2 PSF Extraction

The next step in the process was to extract a Point Spread Function (PSF) from the lensed quasar system SDSS1650+4251. As stated in the lab manual, this lensed system consists of two quasar images plus the galaxy acting as the lens, however this lens is too faint to be detected using the Enzian camera at the Hoher List 1m telescope. Due to the atmospheric seeing conditions the two images of the lensed quasar are blended [8].

In order to extract the PSF of the lensed system, it was first necessary to identify stars present in the coadded science frame, henceforth simply referred to as the science frame, and from these stars measure the seeing. The full width half max (FWHM) of the tars was measured using *iraf*, the software package for astronomical image reduction and analysis. Using the *imexam* task included in the software package, the FWHM of stars and galaxies were found. After analysing a number of objects of both types it was

found that the FWHM was constant for all stars but varied in value for galaxies. This was due to the fact that stars are point sources while galaxies are extended sources of light.

The differences between the two types of sources becomes more evident when the plots and profile made using *iraf* are compared. As can be seen in Figures 6a and 6b, which show the radial profile of a star and a galaxy, the star has a much steeper slope and also that the data points much more closely fit the curve than that of the galaxy. Also from Figures 6c and 6d, which show a contour map of the regions containing the sources, that the contour for the star is much more clearly defined, being made of near concentric circles, while the map for the galaxy is much more noise and the galaxy can barely be seen at all.

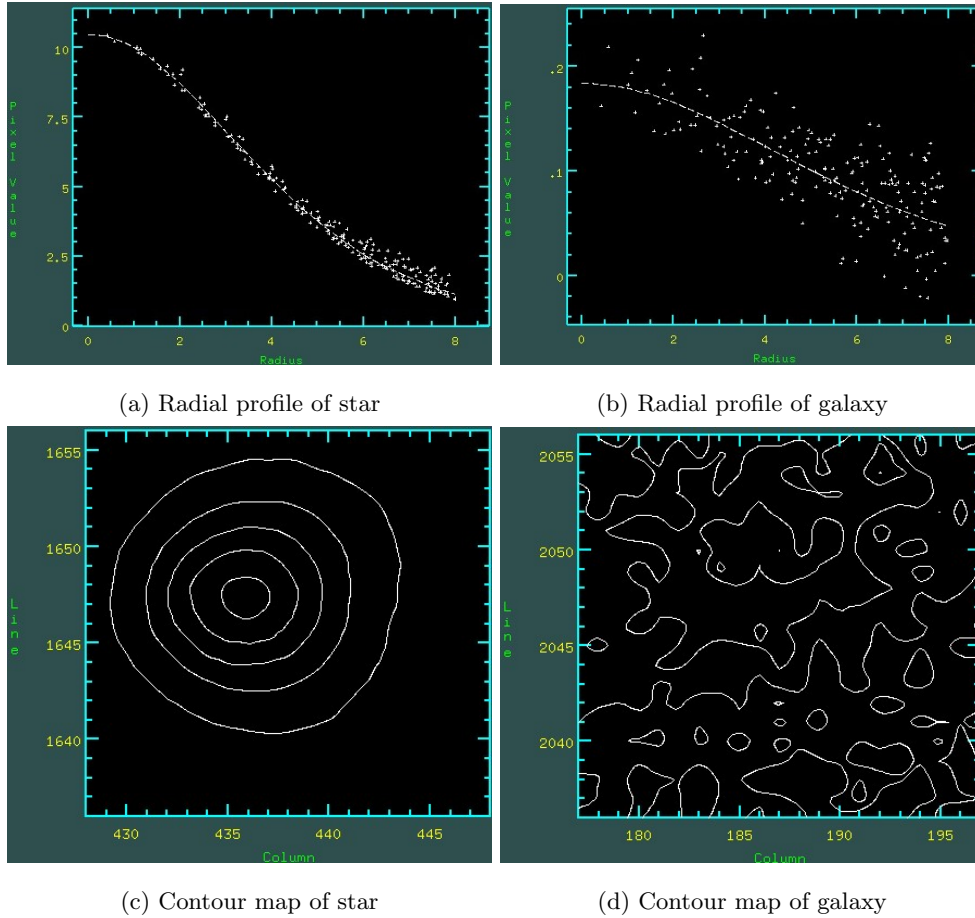


Figure 6: Plots of sample star and galaxy made using *iraf*.

When the plots from the stars are compared to the same plots made from the target lensed quasar system, shown in Figure 7, there are differences that can be observed. The radial profile of the target does not fit the curve as well as the star at larger radii. Also the contour map is not as clean, with the contour lines being deformed and warped, unlike the smoother lines from the star. This indicated that the target is not a point source like the stars but instead may be made up of two objects located very close together.

It was necessary to create a PSF model using five single stars present in the image and a stack. This PSF model could then be used to perform component fitting photometry. The PSF model was created

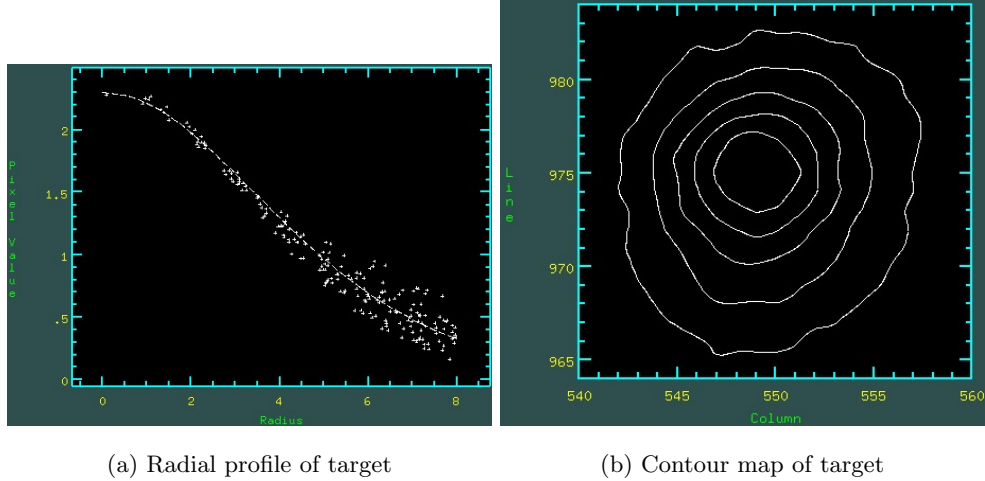


Figure 7: Plots of target made using *iraf*.

using a shell script provided. This script required an ASCII file of stars brighter than the lensed system in the image, a radius which is selected to be large enough to include the outer edges of the light profiles of stars but not so large that it includes light from neighbouring sources, and a maximum size of the PSF, which must be smaller than the lensed system. This script provides an image of each cut out star, scaled so that they all have the same flux, and also an image of all the stacked PSF. Each of the individual star cut outs were visually inspected in order to determine if there was any contribution from light from nearby objects.

The FWHM of the stacked image was measured and found to be 8.08. Contour and surface plots were created of the stacked image and the individual stars. These plots are shown in Figure 8. For the next step in the analysis process, the component fitting, the stacked PSF model was used as it was deemed to be smoother, more concentric and closer to the ideal distribution

### 3.3 Component Fitting

The two lensed images are separated by a very small angular separation, however, it is still possible to decompose the apparent single source into its two component sources and derive photometric data from them. This was done using the 2D fitting program *galfit*, which can simultaneously fit the positions and fluxes of multiple components.

The first step in this process was to add back the sky background that was removed in Section 3.1.2. This was done by extracting the sky values from the FITS files created after the *background* PG in the reduction process. The average of the modes in the second output column was calculated and then normalised to an exposure time of 1 second. This sky background level was then added to the stamp image of the lens system.

The parameter file of *galfit*, was then amended to include the changes specified in Appendix B of the lab manual[8]. The positions of the components were estimated visually using ds9, and the pixel values of these estimates were used to set up the PSF fit of the two components.

After running *galfit*, four images were generated, an empty image, the original, the modelled and the

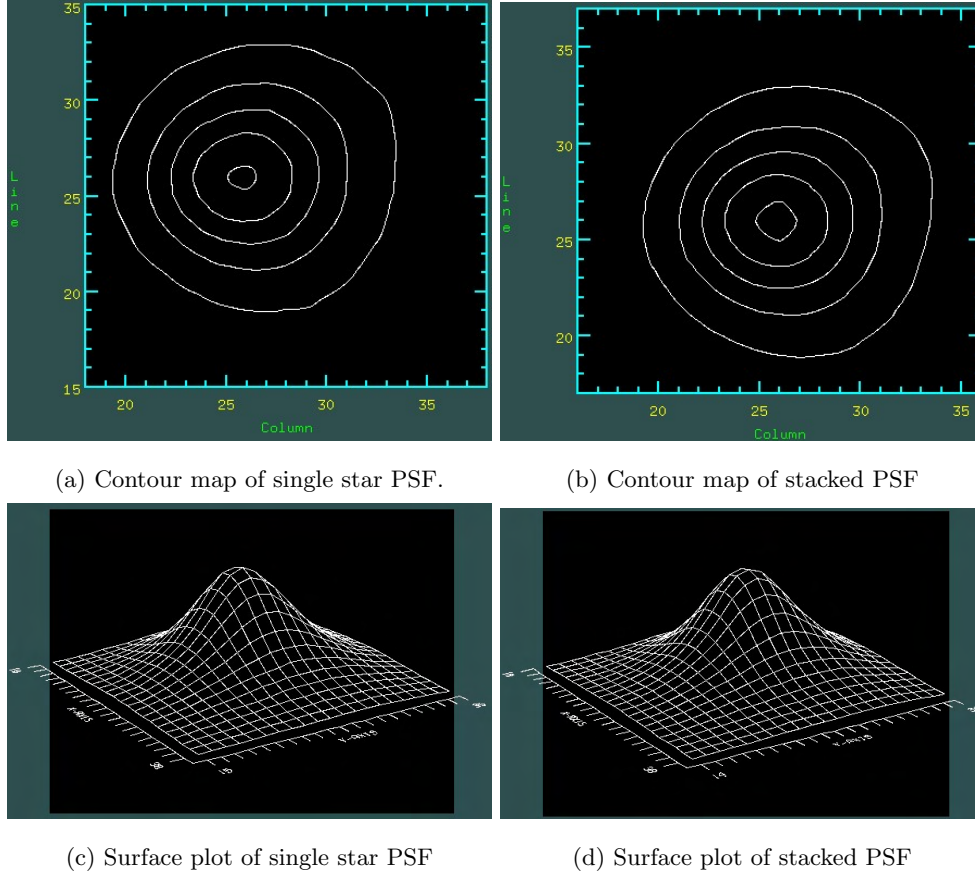


Figure 8: Surface plots and contour maps of a single star PSF and of the stacked PSF, made using *iraf*.

residual image. These are shown in Figure 9. It can be seen from Figure 9d that the two component PSF fit was carried out effectively as there is no structure visible in the image. The inputs used for *galfit*, and the outputs it produced are displayed in Table 1.

	Parameter	PSF 1	PSF 2
Input	x coordinate	26	30
	y coordinate	19	30
	Magnitude	14	14
Output	x coordinate	$24.68 \pm 0.06$	$26.12 \pm 0.01$
	y coordinate	$19.78 \pm 0.08$	$26.28 \pm 0.01$
	Magnitude	$19.20 \pm 0.02$	$17.51 \pm 0.00$

Table 1: Inputs and outputs for running *galfit* using the two component fitting. Coordinates are given in pixels.

From the results of running *galfit*, the magnitude difference between the two images was calculated.

$$\Delta m = m_2 - m_1 \quad (47)$$

$$= 17.51 \pm 0.00 - 19.20 \pm 0.02 \quad (48)$$

$$= -1.69 \pm 0.02 \text{ mag} \quad (49)$$

From this magnitude difference, the flux ratio between the two images could be calculated.

$$\frac{F_2}{F_1} = 10^{-0.4\Delta m} \quad (50)$$

$$= 10^{-0.4(-1.69 \pm 0.02)} \quad (51)$$

$$= 4.74 \pm 0.03 \quad (52)$$

The image separation was first calculated in terms of pixels and then converted to angular separation using the conversion of 0.18 arcsecs per pixel. The uncertainty was calculated using Gaussian uncertainty propagation.

$$s = \sqrt{(x_2 - x_1)^2 + (y_2 - y_1)^2} \quad (53)$$

$$= \sqrt{(26.12 \pm 0.01 - 24.68 \pm 0.06)^2 + (26.28 \pm 0.01 - 19.78 \pm 0.08)^2} \quad (54)$$

$$= 6.66 \pm 0.08 \text{ px} \quad (55)$$

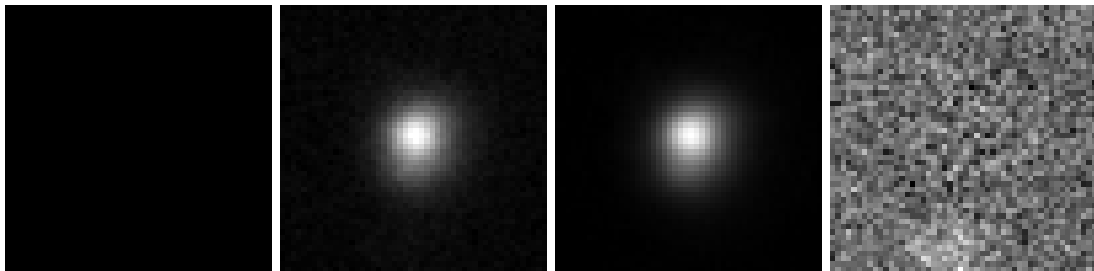
$$= 1.20 \pm 0.01 \text{ arcsec} \quad (56)$$

Using Equation (36), derived in the in the preparatory tasks, the Einstein radius of the lensing system could be determined.

$$s = 2\theta_E \implies \theta_E = \frac{1}{2}s \quad (57)$$

$$\theta_E = 0.60 \pm 0.01 \text{ arcsec} \quad (58)$$

$$= 2.91 \pm 0.04 \times 10^{-6} \text{ rads} \quad (59)$$



(a) Empty image      (b) Original image      (c) Modelled image      (d) Residual image

Figure 9: Output images from *galfit* after running the two component PSF fit.

There is no possibility that the target is one single source, as when this process was repeated with just one PSF and the sky background to fit the lensed system, the residual image contained significant structure, shown in Figure 10d. This structure in the residual indicates that the system was not well fit.

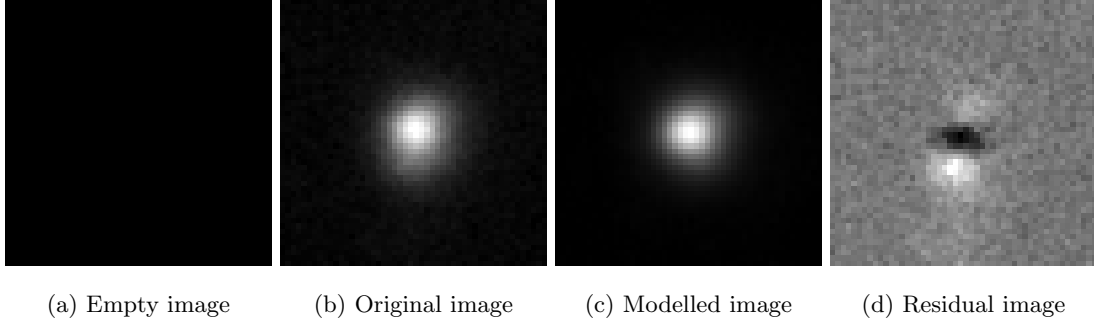


Figure 10: Output images from *galfit* after running the two component PSF fit.

### 3.4 Time-Delay Estimation

The time delay estimation for SDSS1650+4251 was carried out using a separate data set, which was also used for the same purpose by Vuissoz et al. (2007)[12], and it is from this paper that the method used in this section originates. This data set is composed of the magnitudes of the lensed images over a period of time greater than a year.

The lightcurves were first plotted and visually inspected, shown in Figure 11. The large gap in the middle of the lightcurve where there are no observations, lasting slightly over 100 days is likely caused by the target being below the horizon, and therefore not visible during this period. It was not possible to obtain and estimate for the time delay between the two images simply by looking at this plot.

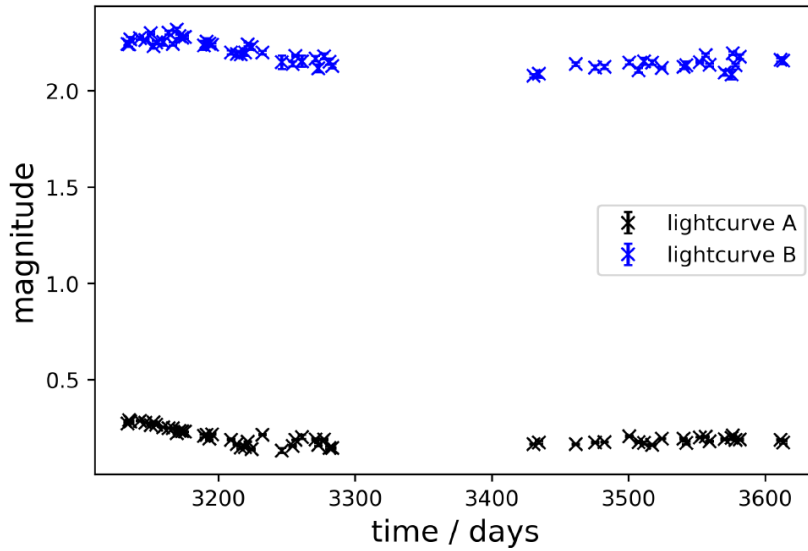


Figure 11: Lightcurves generated from the data set. Time given in heliocentric Julian date

In order to obtain an accurate estimate of the time delay between the two images the minimal dispersion method was implemented using the *tdel* script. This script requires an input of parameters which constrain the magnitude shift intervals and the range and step size of the time delay values that are tested. The script estimates the time delay in three steps. Firstly, the mean magnitudes of the lightcurves are estimated by beginning with an initial guess for the time delay. The mean magnitudes are

calculated only from the overlapped region of the original and shifted lightcurve. These mean values are then used to refine the time delay estimates. This process repeats until a specified accuracy is obtained, set in the parameter file. This only provides an improved estimate for the time delay, not the true time delay as it minimises a noisy dispersion spectrum and therefore it is likely that the value provided for the time delay is a false minimum caused by a noise feature.

The next step in this process was to vary the magnitude shift between the two lightcurves, once again with the variation set using the parameter file. For each value of the noise the program computes a dispersion spectrum and does a second order polynomial fit to smooth out the noise. This provides an improved value for the time delay.

The third and final step is to use a Monte-Carlo strategy in order to obtain the error of the time delay value. This is done by modelling Gaussian noise to each data point in the lightcurves. The time delay is then estimated again a number of times using these new data points. The program computes the mean and variance of these simulated data time delays.

The first estimate of the time delay that was used was a value of 33.7 days. After varying the magnitude shift between the two lightcurves this was improved to 37.0165 days. After running the Monte-Carlo strategy a value of  $36.7 \pm 4.6$  days was obtained.

### 3.5 Lensing Analysis

The final step in the analysis of the lensed quasar SDSS1650+4251 was using findings made in previous sections to determine a value for the Hubble Constant,  $H_0$ . In order to do this a model for the lens had to be chosen. The model chosen for this analysis was the Singular Isothermal Sphere (SIS), as this is the most accurate model that can be handled analytically. The values of redshift for the quasar  $z_s = 1.547$ , and of the lensing galaxy  $z_d = 0.577$  were given by the lab manual [8]. Using the standard cosmological model ( $\Omega_m = 0.3$  and  $\Omega_\Lambda = 0.7$ ), Equation (9) which gives the angular diameter distance of a source as seen by an observer at a different redshift can be solved to find the comoving distances of the two objects,  $w(z_d) = 0.4985 \text{ c}/H_0$  and  $w(z_s) = 1.039 \text{ c}/H_0$ .

In order to calculate the velocity dispersion of the lensing galaxy from the measured image separation, it was necessary to convert the comoving distances to angular diameter distances which was done using Equation (8), and assuming a value of  $H_0 = 71 \pm 4 \text{ km Mpc}^{-1} \text{ s}^{-1}$  [11].

$$D_d = \frac{1}{1 + z_d} w(z_d) \quad (60)$$

$$= \frac{0.4985}{1 + 0.577} \frac{3 \times 10^5 \text{ kms}^{-1}}{71 \text{ kmMpc}^{-1} \text{ s}^{-1}} = 1336 \text{ Mpc} \quad (61)$$

$$D_s = \frac{1}{1 + z_s} w(z_s) = 1724 \text{ Mpc} \quad (62)$$

$$D_{ds} = \frac{1}{1 + z_s} [w(z_s) - w(z_d)] = 897 \text{ Mpc} \quad (63)$$

The separation between the images, and the Einstein radius for the system were found in the previous section. Equation (25), which describes the characteristic angular scale of a lens could then be rearranged

to find the value for the velocity dispersion, and the values found above plugged in.

$$\theta_E = 4\pi \left( \frac{\sigma_v}{c} \right)^2 \frac{D_{ds}}{D_s} \implies \sigma_v = c \sqrt{\frac{\theta_E}{4\pi} \frac{D_s}{D_{ds}}} \quad (64)$$

$$\sigma_v = c \sqrt{\frac{2.91 \pm 0.04 \times 10^{-6} \text{ rads}}{4\pi} \frac{1724 \text{ Mpc}}{897 \text{ Mpc}}} \quad (65)$$

$$= 200 \pm 25 \text{ km/s} \quad (66)$$

The projected mass inside of the Einstein radius could then be calculated. Using Equations (26) and (18), the critical convergence and subsequently the projected mass could be calculated.

$$\Sigma_{cr} = \frac{c^2}{4\pi G} \frac{D_s}{D_d D_{ds}} \quad (67)$$

$$= 2.39 \times 10^{15} \text{ M}_\odot / \text{Mpc}^2 \quad (68)$$

$$M(\theta < \theta_E) = \pi \theta_E^2 D_d^2 \Sigma_{cr} \quad (69)$$

$$= 1.13 \pm 0.03 \times 10^{11} \text{ M}_\odot \quad (70)$$

This value obtained for the projected mass of the lens inside of the Einstein radius seems reasonable as they fall into the normal range of masses for galaxies, which typically range in mass from  $\sim 10^7$  to  $10^{12} \text{ M}_\odot$  [11].

The next task in this analysis process was to compute the position of the lens galaxy and derive an estimate for the Hubble Constant,  $H_0$ . This was done using the flux ratio of the images, which was found in Equation (50). This flux ratio was assumed to be identical the magnification ratio which was determined in Equation (39) of the preparatory tasks.

$$\Gamma = \frac{\mu_+}{\mu_-} = \frac{1 - \theta_E/\theta_-}{1 - \theta_E/\theta_+} = \frac{F_2}{F_1} \quad (71)$$

For SIS system, the image separation is given by Equation (36),  $s = \theta_- - \theta_+ = 2\theta_E$ . Therefore, the above equation can be rearranged to obtain the following relations.

$$\theta_- = \frac{2\theta_E}{\Gamma - 1} \quad \theta_+ = \theta_- - 2\theta_E \quad (72)$$

$$\Delta\theta_- = \sqrt{\left( \frac{2\Delta\theta_E}{\Gamma - 1} \right)^2 + \left( \frac{2\theta_E \Delta\Gamma}{(\Gamma - 1)^2} \right)^2} \quad \Delta\theta_+ = \sqrt{(\Delta\theta_-)^2 + (2\Delta\theta_E)^2} \quad (73)$$

$$\theta_- = 0.321 \pm 0.006 \text{ arcsecs} \quad \theta_+ = -0.88 \pm 0.02 \text{ arcsecs} \quad (74)$$

The negative value for  $\theta_+$  implies that the two images are on opposite sides of the lens. The pixel coordinates of the lensing galaxy could then be found by transforming from the position of one image to another with the matching fraction of image separation.

$$\vec{X} = x_1 + \frac{1}{\Gamma}(x_2 - x_1) = 24.93 \pm 0.07 \text{ px} \quad (75)$$

$$\vec{Y} = y_1 + \frac{1}{\Gamma}(y_2 - y_1) = 20.91 \pm 0.09 \text{ px} \quad (76)$$

After the position of the galaxy is found it is possible to obtain an estimate for the value of the Hubble Constant,  $H_0$ . This is done by beginning with the equation for the time delay derived in the preparatory



tasks, given in Equation (43), and manipulating and rearranging so that the Hubble constant is given in terms of values already previously determined.

$$\Delta t = \frac{1+z_d}{c} \frac{D_d D_s}{D_{ds}} \cdot \theta_E (|\theta_-| - |\theta_+|) \quad (77)$$

$$= \frac{1}{c} \frac{x(z_d)x(z_s)}{x(z_s) - x(z_d)} \cdot \theta_E (|\theta_-| - |\theta_+|) \quad (78)$$

$$= \frac{1}{H_0} \frac{0.4985 \cdot 1.039}{1.039 - 0.4985} \cdot \theta_E (|\theta_-| - |\theta_+|) \quad (79)$$

$$H_0 = \frac{1}{\Delta t} \frac{0.4985 \cdot 1.039}{1.039 - 0.4985} \cdot \theta_E (|\theta_-| - |\theta_+|) \quad (80)$$

$$= 73.4 \pm 5 \text{ kmMpc}^{-1} \text{ s}^{-1} \quad (81)$$

This value obtained for the Hubble constant agrees with some of the most recent values for the Hubble constant, which found it to be  $H_0 = 73.04 \pm 1.04 \text{ kmMpc}^{-1} \text{ s}^{-1}$ , using Cepheids and SNe Ia [10]. However it is important to note that there is great variance when it comes to the values obtained for the Hubble constant, especially across various measurement techniques.



Figure 12: Object positions in lensing system. A and B are the quasar images and G is the lensing galaxy.  
Source: Lab Manual[8]

An analysis of this lensed quasar system was previously carried out by Morgan et al. (2003) [7]. It was from these observations, made using the Kitt Peak National Observatory 3.5m Telescope, that the positions illustrated in Figure 12 were derived. When compared to the positions found from the analysis carried out above, it can be concluded that the positions obtained were unrealistic and this is mainly due to the model for the lensing system used. In this lab course an axisymmetric Single Isothermal Sphere model was used. While this model is useful as it can be solved analytically, it has its limitations, such as it assumes that the lensing galaxy is located on the line between the two images. It can be seen from the work carried out in Morgan et al. that this is not the case.

## Part I

# Night-Time Observations of an Exoplanet Transit

## 4 Theory

### 4.1 Exoplanets

It was only in 1992 that the first exoplanets were discovered by Wolszezan and Frail (1992) [13]. These first exoplanets were discovered by noticing anomalies in the period of pulsation of the pulsar around which they orbit. It was three years later, in 1995, that the first exoplanets were discovered around a main sequence star [6]. Since these early days of exoplanet discovery, over 4300 more exoplanets have been discovered [1].

#### 4.1.1 Exoplanet Discovery Methods

The majority of stars are located at such large distances, that they cannot be spatially resolved and act as point sources. Due to this, it is not usually possible to directly observe or image any exoplanets orbiting around their host star using direct techniques such as direct imaging or gravitational microlensing.

Exoplanets are therefore usually discovered by studying the effect they have on the light coming from their host star using indirect methods such as the radial velocity technique and the transit method. While exoplanets have been discovered using all the methods mentioned above, the transit method has led to the most discoveries [1].

More than 99% of the exoplanets discovered to date are massive planets, larger than any planet in our Solar System, and orbit close to their host star with a short period. It is important to remember that these discovered exoplanets are only a subset of all the exoplanets out there in space and that this subset is heavily biased due to the detectability factors of the detection methods [5].

The transit method, also called transit photometry, is the most popular method for exoplanet discovery. This method requires the orbital plane of the exoplanet to be near or along the line of sight. As the exoplanet passes in front of the host star, a small amount of light from the star is blocked and the star appears to get dimmer. Using precise measurements of the fluctuations of stellar brightness as a function of time, exoplanet transits can be distinguished by their periodicity and shape, from other intrinsic solar brightness variations such as star spots.

The change in stellar flux,  $\Delta F$ , over the total flux,  $F$ , can give an estimate on the ratio between the radius of the host star to radius of the exoplanet. The relationship is given by:

$$\frac{\Delta F}{F} = \frac{R_P^2}{R_\star^2} \quad (82)$$

where  $R_P$  is the radius of the exoplanet and  $R_\star$  is the radius of the host star. This does not confirm that the change in flux was caused by an orbiting exoplanet, only that there is a Jupiter sized opaque body

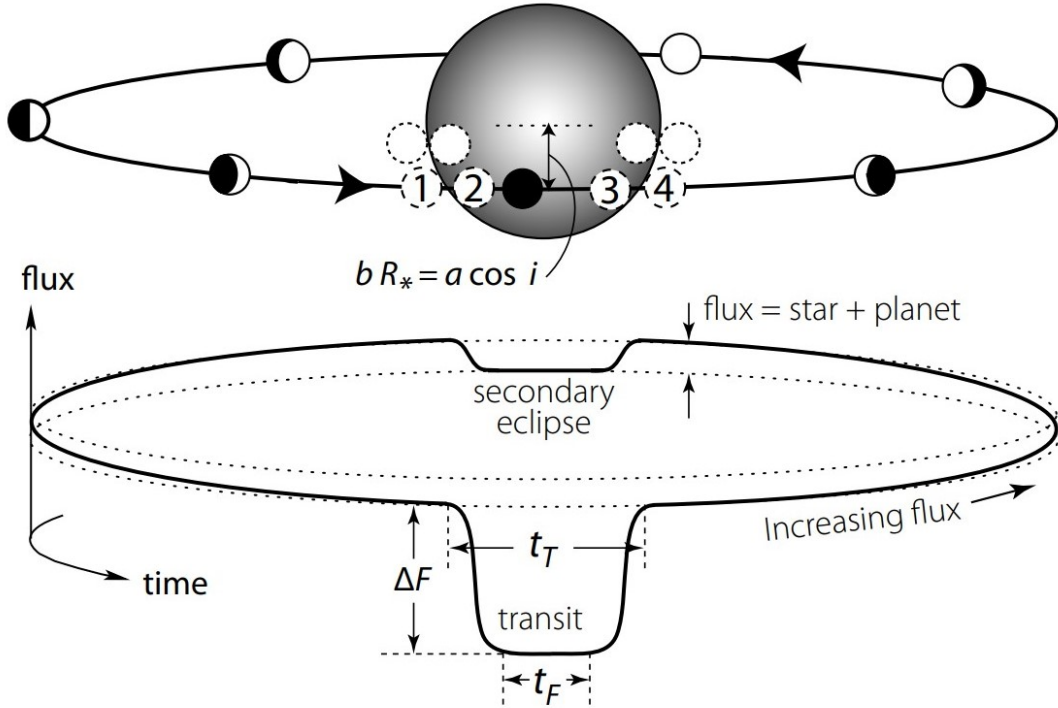


Figure 13: Illustration of the variation in stellar flux as a function of orbital phase for a transiting exoplanet. [9]

orbiting the star. To confirm that the body is an exoplanet and not, for example, a brown dwarf star, the mass of the transiting body needs to be found. This can be done using the radial velocity technique [3].

#### 4.1.2 Geometry of Transits

For the transit of an exoplanet to be observed, the orbit normal must be nearly perpendicular to the line of sight (i.e.  $i \approx 90^\circ$ ). If a planet of radius  $R_P$  orbits a star of radius  $R_*$ , at a distance of  $a$ , the probability of observing a transit of a randomly orientated planet is given by [3]:

$$P_{\text{tr}} = \frac{R_* + R_P}{a} \approx \frac{R_*}{a} \quad (83)$$

This equation shows how the transit method strongly selects for large exoplanets that orbit very closely to their host star. For example, the probability of detecting an exoplanet at the same orbital radius as Jupiter (5.2AU) transiting a solar radius star is approximately 0.09%, while if it orbited at the typical radius of a hot-Jupiter exoplanet (0.05AU) the probability of detection increases to 9%.

Another important geometric factor in transits is the impact parameter,  $b$ , which is defined as the shortest distance from the center of the stellar disc to the path of the planet, as shown in Figure 13.

When describing the phases of an exoplanet transit, there are four important points or contacts. The first contact is when the limb of the planetary disc first coincides with the stellar disc and the stellar flux begins to decrease. The stellar flux continues to decrease until the second contact, which is the point where all of the planetary disc is just within the stellar disc. The stellar flux remains constant until the

third contact, which is the last point at which the planetary disc is fully within the stellar disc. The stellar flux then rises again until the fourth contact, when the planetary disc is completely passed the stellar disc. These contacts are illustrated in Figure 13.

The total transit time,  $t_T$ , is defined as the time between the first and fourth contacts. For an exoplanet system with impact parameter  $b = 0$ , and radii  $R_\star \gg R_P$ , the total transit time is given by [3]:

$$t_T \approx \frac{PR_\star}{\pi a} \quad (84)$$

From the transit method, the mass and radius of the orbiting exoplanet can be calculated.

## 5 Preparatory Tasks

### 5.1 Source Selection

The observations of the exoplanet transit took place on the night of August 24<sup>th</sup> 2022. Using the Exoplanet Transit Database a list of possible observing targets was chosen[2]. The finding charts and visibility plots were then made for the targets so that the optimal target could be chosen. The optimal target was chosen according to a number of criteria. Firstly the target must be located relatively high in the sky during the period of the transit. This is for two reasons, firstly, the AIFA telescope has an operating limit where it cannot be lowered further than 20° from the horizon without risking damage to the instrument. Secondly, the higher in the sky the target is located, the less air the light must travel through, improving the quality of the observations. Another criteria relevant to the target selection is the magnitude of the target. Given the type of telescope, the sensitivity of the CCD, and atmospheric limitations from the geographic location of the AIFA, the targets must have magnitudes of 12 or brighter. Another criteria relevant to target selection is the twilight times and times of transit. the transit of the exoplanet must not be during the twilight times and there must be at least 30 minutes each side of the transit in order for the baseline brightness of the star to be measured. The location of the moon is also an important factor to consider, preferably the target is on the opposite side of the sky as the moon. Given these restrictions, the target TOI 1461.1b was chosen to be the target for these observations. TOI 1461.1b has a magnitude of 11.8, and a transit lasting 154 minutes. On the night of the observations the transit began at 22:54, centred at 00:11 and ended at 01:28 (Universal Time).

## 6 Observations

Before beginning the observations of the exoplanet transit, the telescope was set up. The covers protecting the mirrors were removed and the CCD camera attached and focused. The cooling of the CCD was turned on and allowed to reach temperature. Ten twilight flats were then taken, with 40 second exposure, however, twilight was nearly over, making them ineffective, so dome flats were also taken at the end of the observations. This exposure time was chosen so that all the pixels were adequately illuminated, but without over saturating any of the pixels.

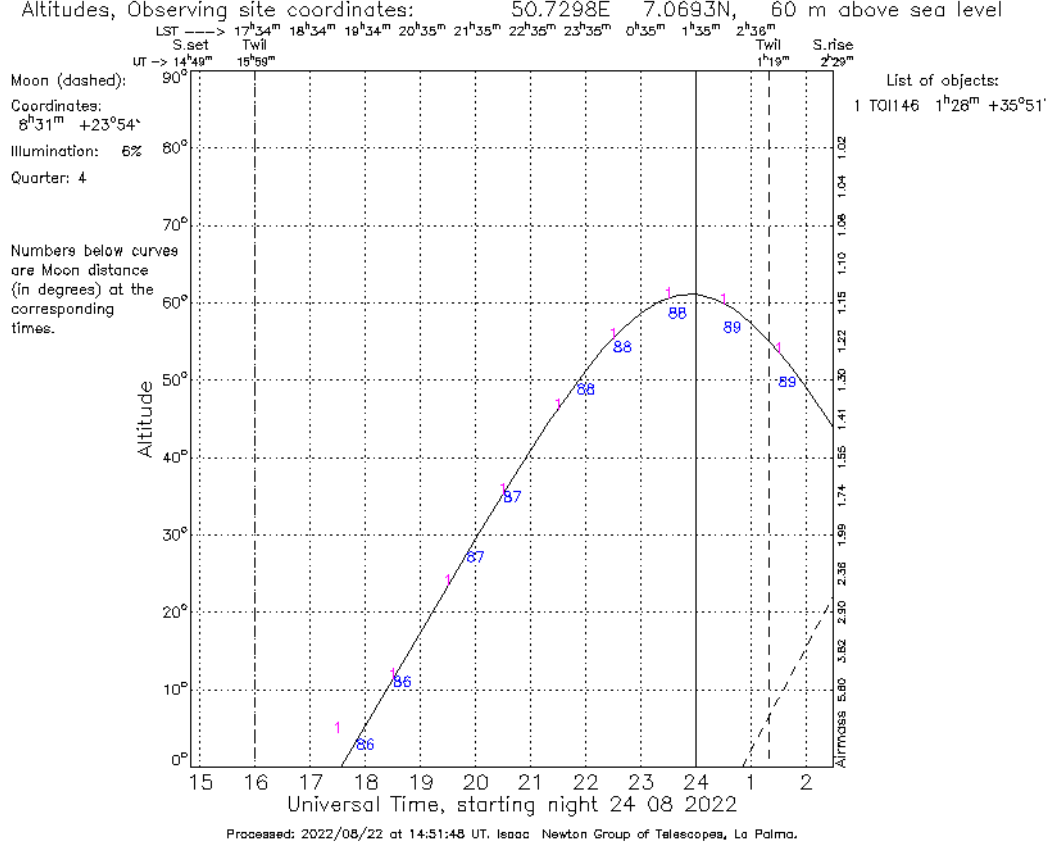


Figure 14: Visibility plot for the target on the night of the 24<sup>th</sup> of August 2022.

The pointing of the telescope was then calibrated. This was done by observing three bright reference stars, with known positions. This step ensures that when coordinates are inputted to the telescope mount driver, that the telescope is actually pointing correctly at those coordinates.

After this, the telescope was pointed at the target and a few test frames were taken. These frames were compared against the finding charts to ensure that the telescope was properly pointing at the target. Figure 15, shows the finding chart used and a sample science frame, both with the target star highlighted. Note that the finding chart was inverted along the horizontal axis so that both images have the same orientation, making the target easier to identify against the background stars.

After this the bias and dark frames were taken. Twenty bias frames were taken with zero second exposure. Then twenty dark frames were taken with a thirty second exposure. After these calibration frames were taken the telescope could be pointed at the scientific target and the science frames taken. Unfortunately, the full transit could not be observed due to time restrictions. Instead measurements were taken from the middle of the transit until approximately fifteen minutes after the transit was complete. In total over 120 exposure of 30 seconds were taken. After the science frames were taken, 20 dome flats were taken with a 31 second exposure time. This was done by pointing the telescope at a white screen located on the inside of the dome, which was uniformly illuminated using a lamp.



were split into folders for each image type, bias, dark, flat and science frames. Please see the data reduction section from the first part of this report for a more detailed instruction on the steps involved. The only differences in this process was that the instrument section in *THELI* would have been set to STL6303@AIfA to match the instrument that was used for observations. Also the dark frames were included this time as the CCD is not cooled by liquid nitrogen and therefore contains a small amount of dark current that must be accounted for. For the *coaddition* PG only the sky subtraction was carried out. Automatic sky modelling was carried out using the starting conditions of DT=1, DMIN=10, SIZE=256.

## 7.2 Astrometry

Unlike for the first part of this lab, the astrometric calibration step was not carried using *THELI*, as neither a very stable astrometric solution nor absolute photometric calibration were needed for this part of the lab course. This is due to the fact that in the later parts of this experiment the exoplanet target was selected by hand, and also only the changes in the targets brightness are needed.

The astrometric calibration was thus carried out using *astrometry.net*. The calibrated science frames were uploaded to the website and processed. *Astrometry.net* matches the sources in the science frames with reference sources and provides an astrometric solution to link the pixel coordinates with sky coordinates. The result FITS files from this calibration were then downloaded from the websites and saved into the working directory of this section. The downloaded files carefully matched with the correct weight image generated by *THELI* in the previous section.

## 7.3 Source Fluxes

The next step in measuring the exoplanet transit, was to carry out a photometric calibration between the various science frames. This is necessary as the brightness variations during an exoplanet transit are typically of the order of 0.01 mag. A number of non-variable stars were chosen as a reference in order to measure the flux variation between frames. These flux variation can be caused by a number of factors such as changing atmospheric conditions or light pollution during the period of observation.

Using the script provided on the computer, *SExtractor* was run in order to create a catalogue for each of the processed science frames. This lists the coordinates of the identified objects and their associated fluxes. The *APER* method was chosen for measuring the flux of the objects. This measures the flux of the objects by estimating the flux above the background inside a circular aperture. An aperture radius of 20 pixels was chosen for this as this was found to be the best value for ensuring that all the objects were enclosed in their measuring circle, while also minimising the background included and overlaps between the regions.

After the catalogue was created a script was run to identify the coordinates of the exoplanet system and a number of reference stars. Ten reference stars were chosen across the frame. These sources and the exoplanet system are shown in Figure 17. These sources were saved to a list for further analysis. Using another script, a time series was created for these reference stars and the exoplanet system. This created



a data table containing the time of each frame, the flux and the flux error of each object in the list.

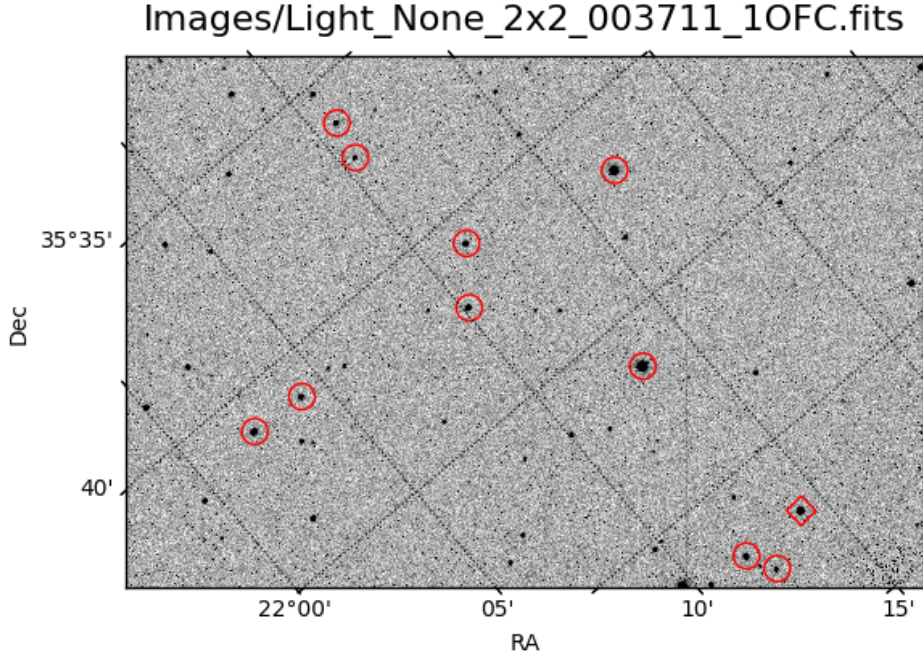


Figure 17: Exoplanet system marked with red square and the reference stars marked with red circles.

The reference stars are needed for this analysis as there are variations in flux between exposures. The reference stars can be used to account for this by finding scaling factors for each frame such that the reference stars have a constant brightness between exposures. A variations of flux for each of the reference stars was visually inspected, to identify ones with reasonable light curves. Some of the stars were deemed unusable as stars due erratic changes in their light curves. From the ten reference stars, two were discarded. Figure 18 shown a sample lightcurve from a good and bad reference star. The remaining reference stars all had similar shapes to their lightcurves, indicating that their variation in flux were all caused by the same effects, not properties of the stars themselves. From the remaining reference stars a weighted mean flux was calculated for each frame using the weighted mean function in the numpy python package. These average fluxes were then used to calculate a scale factor for each frame so that the mean flux of each frame was the same as the first frame.

These scaling factors were then applied to the flux values of the exoplanet system. In principle this should result in all the variations in brightness of the exoplanet system being caused by the exoplanet transit. Figure 19 shows the lightcurve obtained from the exoplanet transit system.

## 8 Results

The exoplanet transit lightcurve obtained in the previous section, Figure 19, shows the general shape expected from an exoplanet transit lightcurve. Figure 20, shows a sample lightcurve of this exoplanet



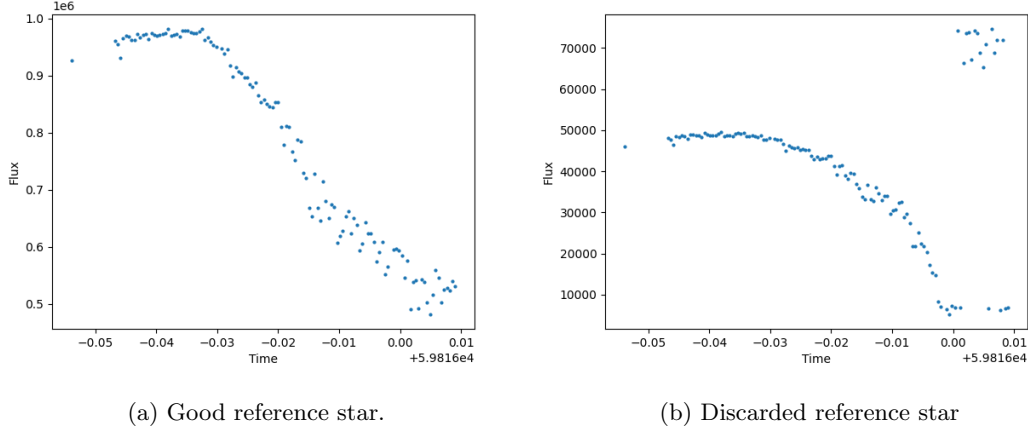


Figure 18: Sample of a good reference star versus a bad reference star.

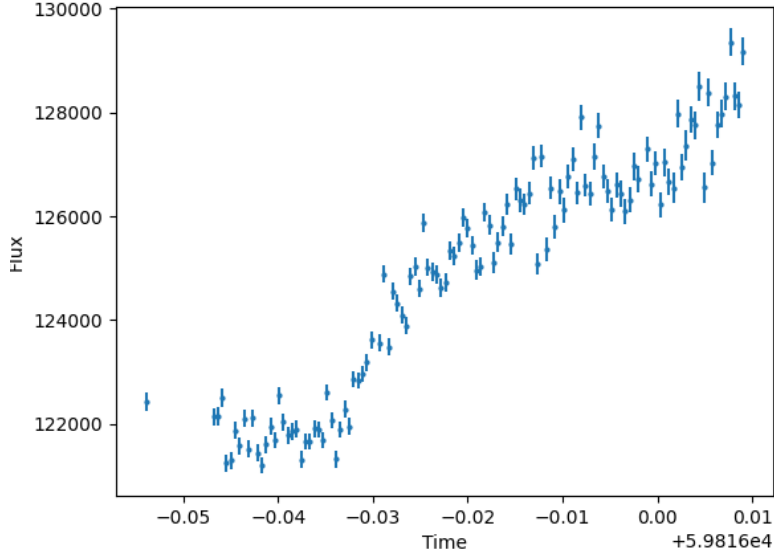


Figure 19: Exoplanet transit lightcurve of TOI 1461.1b.

system made from previous observations [2]. Noting that only the second half of the transit was observed during this lab, it can be seen that there are similarities between the two curves. The flux of the system is relatively flat during transit, until the flux begins to increase as the exoplanet no longer covers the star. This continues until the exoplanet is no longer in front of the star and the flux flattens once more. From the lightcurve obtained from the measurements it can be seen that this flattening of the lightcurve takes place after the exoplanet has moved passed the star, however, after some time the flux begins to increase again. This is likely due to issues with the scale factor obtained for these later frames. It can be seen in Figure 18, that these later frames are quite dark and therefore, the scale factor maybe overcompensating this effect, artificially boosting the measured flux of the exoplanet system. This spike was the ignored for any of the further calculations.

The magnitude depth of the exoplanet transit could be calculated from the values of the scaled

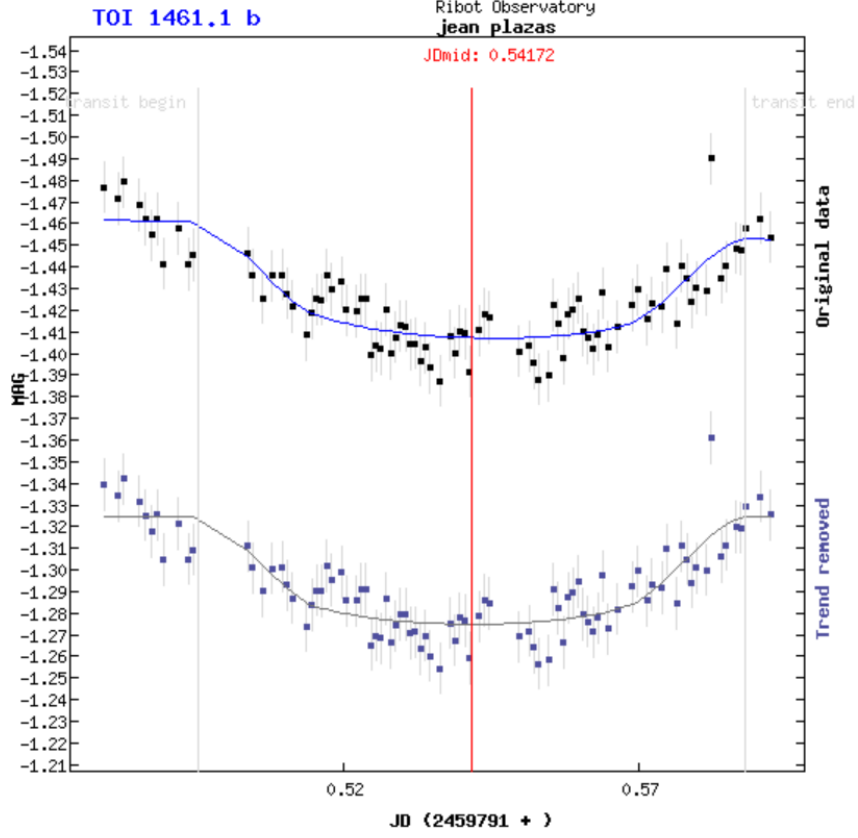


Figure 20: Sample lightcurve of a transit of this exoplanet system from observations made by Jean Plazas at the Ribot Observatory taken on the night of the 30<sup>th</sup> of July 2022 [2].

flux. Mean value of the flux was taken for the flux values during the transit and then again for the flux values after the transit but before the spike near the end of the observation. Using the formula  $m_1 - m_2 = -2.5 \log_{10}(f_1/f_2)$ , the magnitude depth of the transit could be calculated. It was found from the observations made that the system had a magnitude depth of  $0.041 \pm 0.005$ . This is a larger magnitude depth than the value expected from the literature of 0.0226 [2], however it is of the right order of magnitude. This increase in the magnitude depth is likely due to the calculation of the scale factors, leading to the flux values after the transit being overestimated.

Using Equation (82), the ratio between the radius of the exoplanet and the star could be calculated. A value was found of  $0.0187 \pm 0.0002$ . However, it is important to note that this value is likely an overestimation for the same reasons as described above.

## 9 Conclusions

The data from previous observations made of the gravitational lensed quasar SDSS1650+4251 was reduced and analysed to determine the time delay between the different light travel paths in order to constrain the value of the Hubble parameter. It was found that the time delay between the two gravitationally lensed images of quasar SDSS1650+4251 was  $36.7 \pm 4.6$  days. The value for the Hubble parameter was found to be  $H_0 = 73.4 \pm 5 \text{ kmMpc}^{-1} \text{ s}^{-1}$ , which agrees with previous work found in literature.

Using the 50cm Cassegrain telescope in the AIfA the second half of the transit of the exoplanet TOI 1461.1b was observed during the night of the 24<sup>th</sup> of August 2022. After the data reduction was carried out, a lightcurve was obtained which showed the exoplanet transit. From the lightcurve, it was measured that the exoplanet has a transit magnitude depth of  $0.041 \pm 0.005$ , and the ratio between the planet and host star radii is  $0.0187 \pm 0.0002$ . The value obtained for the magnitude depth does differ from the expected value found in the literature. This was likely caused by issues in calculating the scale factor which overcompensates and increases the magnitude of the star for the later frames of the observations.

## References

- [1] NASA Exoplanet Archive. *Retrieved 15 March 2021*. URL: [exoplanetarchive.ipac.caltech.edu](http://exoplanetarchive.ipac.caltech.edu).
- [2] Exoplanet Transit Database of the Czech Astronomical Society. *Retrieved 23 August 2022*. URL: <http://var2.astro.cz/ETD/predictions.php>.
- [3] Carole Haswell. *Transiting exoplanets*. Cambridge: Cambridge University Press, 2010.
- [4] Andrew R. Liddle. *An Introduction To Modern Cosmology*. 1998.
- [5] Jack Jonathan Lissauer and Imke De Pater. *Fundamental planetary sciences : physics, chemistry and habitability*. Updated edition. Cambridge: Cambridge University Press, 2019. ISBN: 9781108411981.
- [6] Michel Mayor and Didier Queloz. “A Jupiter-mass companion to a solar-type star”. In: *Nature* 378.6555 (Nov. 1995), pp. 355–359. DOI: 10.1038/378355a0.
- [7] N. D. Morgan, J. A. Snyder, and L. H. Reens. “SDSS J1650+4251: A New Gravitational Lens”. In: *The Astronomical Journal* 126.5 (Nov. 2003), pp. 2145–2151. DOI: 10.1086/378602.
- [8] *Optical Astronomy and Gravitational Lensing Manual*. AIfA: Bonn University, 2020.
- [9] M. A. C. Perryman. *The exoplanet handbook*. Second edition. Cambridge University Press, 2018. ISBN: 9781108419772.
- [10] Adam G. Riess et al. “A Comprehensive Measurement of the Local Value of the Hubble Constant with 1 km/s/Mpc Uncertainty from the Hubble Space Telescope and the SH0ES Team”. In: *The Astrophysical Journal Letters* 934.1 (July 2022), p. L7. DOI: 10.3847/2041-8213/ac5c5b. URL: <https://doi.org/10.3847/2041-8213/ac5c5b>.
- [11] Peter Schneider. *Extragalactic Astronomy and Cosmology*. 2006.
- [12] C. Vuissoz et al. “COSMOGRAIL: the COSmological MONitoring of GRAvItational Lenses. V. The time delay in SDSS J1650+4251”. In: *Astronomy and Astrophysics* 464.3 (Mar. 2007), pp. 845–851. DOI: 10.1051/0004-6361:20065823. arXiv: astro-ph/0606317 [astro-ph].
- [13] A. Wolszczan and D. A. Frail. “A planetary system around the millisecond pulsar PSR1257 + 12”. In: *Nature* 355.6356 (Jan. 1992), pp. 145–147. DOI: 10.1038/355145a0.